Isolating climatic, tectonic, and lithologic controls on mountain

landscape evolution

- 3 Joel S. Leonard^{1*}, Kelin X. Whipple¹, and Arjun M. Heimsath¹
- ¹School of Earth and Space Exploration, Arizona State University, Tempe, Arizona, USA
- *Corresponding Author: Joel S. Leonard (joel.leonard@asu.edu)
- 6 Abstract

1

2

- 7 Establishing that climate exerts an important general influence on topography in tectonically active
- 8 settings has proven an elusive goal. Here, we show that climates ranging from arid-humid consistently
- 9 influence fluvial erosional efficiency and thus topography, and this effect is captured by a simple
- metric that combines channel steepness and mean-annual rainfall, k_{snO} . Accounting for spatial
- 11 rainfall variability additionally increases sensitivity of channel steepness to lithologic and tectonic
- controls on topography, enhancing predictions of erosion and rock uplift rates, and supports the
- 13 common assumption of a reference concavity near 0.5. In contrast, the standard channel steepness
- metric, k_{sn} , intrinsically assumes climate is uniform. Consequently, its use where rainfall varies
- spatially undermines efforts to distinguish climate from tectonic and lithologic effects, can bias
- 16 reference concavity estimates, and may ultimately lead to false impressions about rock uplift patterns
- 17 and other environmental influences. Capturing climate is therefore a precondition to understanding
- 18 mountain landscape evolution.
- 19 Teaser
- 20 Accounting for climate unlocks potential to disentangle primary factors controlling the evolution of
- 21 mountain topography.

22 INTRODUCTION

- 23 Covariation among climate, tectonics, and lithology is common in mountain landscapes, and has long
- 24 confounded attempts to isolate and quantify their respective roles in moderating topography and erosion
- 25 (1-3). Climate's role in particular has been the subject of vigorous debate and clearly determining whether
- climate importantly influences topography remains a critical challenge (1, 4-8). In principal, the normalized
- channel steepness index (k_{sn}) , a widely used metric that has produced useful correlations with erosion on
- 28 millennial timescales in diverse settings, has the potential to detect such an influence (1-3). However, a key
- limitation of k_{sn} is its reliance on upstream drainage area as a discharge proxy, thus building in an
- 30 assumption of spatially uniform rainfall.

A promising alternative to k_{sn} is the variant, $k_{snO}(1)$:

$$k_{snQ} = SQ^{\theta_{ref}},\tag{1}$$

where S is river slope, Q is water discharge, and θ_{ref} is the reference concavity index. k_{snQ} is a generalized version of similar metrics (e.g., ref(9, 10)) that uses the product of drainage area (A) and average upstream rainfall (\bar{P}) estimated from mean-annual rainfall (MAP) as an improved discharge proxy (I). Importantly, this allows k_{snQ} to account for spatial rainfall variability (II). Although the stochastic natures of storms and floods are not captured, MAP resolves spatial patterns well and scales quasi-linearly with larger geomorphically relevant discharges (I2). To the extent MAP captures the principal influence of climate, its near global coverage and relative simplicity offer notable advantages over reliance on sparse stream gauges. A critical test to evaluate the usefulness of incorporating MAP is comparing the capacities of k_{sn} and k_{snQ} to predict erosion rates where rainfall is spatially variable.

Here, we present a detailed, large-scale analysis of topography as represented in river profiles and 10 Be erosion rates from the northern central Andes of Peru and Bolivia (Fig. 1) testing the hypothesis that k_{snQ} is a better predictor of erosion rates than k_{sn} (I, II). In so doing, we highlight assumptions implicit to each metric and quantitatively evaluate the implications of carrying forward these different sets of assumptions on understanding of the roles of climate, tectonics, and lithology on landscape evolution. This landscape is characterized by a ~20-50 km wide band of high topographic relief and experiences a dramatic regional, but locally variable, orographic rainfall gradient that spans much of the global range of mean-annual rainfall. High elevations typically receive <~0.25 m/yr while lower elevations experience ~3–6 m/yr of rainfall. The study area spans >1500 km along-strike, and in addition to extreme climate variations, encompasses diverse tectonics (e.g., variable subduction geometry and seismicity)(I3, I4) and lithology (I5, I6). This degree of complexity is common in tectonically active ranges and is ideal for comparing the abilities of k_{sn} and k_{snQ} to extract meaningful information about primary drivers of landscape evolution.

River Incision Theory and Metrics

A common framework for interpreting k_{sn} and k_{snQ} is the stream power model (SPM). The SPM can be cast in terms of drainage area (A) or discharge (Q):

$$E = KA^m S^n, (2a)$$

$$E = K_p Q^m S^n, (2b)$$

$$K = K_n \bar{P}^m, \tag{2c}$$

- where E is erosion rate (equal to the uplift rate (U) at steady state); K and K_p are erosional efficiency
- coefficients; and m and n are positive constant exponents that depend on and erosional process mechanics
- and runoff variability (1, 2, 17). Dependence on runoff variability and erosional thresholds more broadly
- suggests n ought vary with climate (2, 12, 18-23). Importantly, however, the primary influence of climate
- 64 is encapsulated within K, along with myriad other factors (e.g., rock properties). By contrast, K_p is in
- principle independent from rainfall, and to the extent that rainfall is the primary relevant component, climate
- 66 (1, 11). Effects of other factors like rock properties, weathering, sediment flux and size, and vegetation that
- do not scale with rainfall are still subsumed in K_p (17, 24–28).
- Interpreting channel steepness patterns requires knowledge of the reference concavity index, θ_{ref} , which
- describes scaling between discharge and channel slope and allows comparisons between rivers of different
- sizes (29). Values near 0.5 are expected from theory and under uniform conditions $\theta_{ref} = m/n$ (2, 30, 31).
- 71 However, spatially and/or temporally variable conditions affect profile concavity and channel steepness
- 72 (11, 32–35).
- River profile collinearity in χ -elevation plots (χ -z) has become a popular method to determine optimal θ_{ref}
- values from topography (34, 36, 37). This method leverages the SPM prediction that, provided θ_{ref} is set
- appropriately, the χ -transform linearizes river profiles adjusted to uniform conditions with slopes equal to
- 76 k_{sn} (34). Assuming rivers of varying sizes are adjusted to uniform conditions, the optimal θ_{ref} that best
- approximates m/n is that which minimizes differences among profile slopes (34, 36, 38, 39). Collinearity
- 78 can be quantified by comparing k_{sn} values and optimized by minimizing variability (disorder) in χ -z (36,
- 79 38, 39). However, where either rainfall or rock erodibility vary spatially (a common condition), the θ_{ref} that
- best achieves collinearity among profiles may not be meaningful.
- We can evaluate the effect of rainfall on collinearity by modifying χ to scale with Q (i.e., $\bar{P} \cdot A$), which we
- define as $\chi_Q(11, 34, 40)$ (see Materials and Methods). The slope of river profiles on χ_Q -z plots is k_{snQ} .
- 83 Therefore, spatial variations in rainfall that drive differences in channel steepness should not affect
- 84 collinearity in χ_{O} -z, improving θ_{ref} estimates provided catchments are adjusted to the rainfall pattern.

RESULTS AND DISCUSSION

86 River Profile Analysis

- 87 Transversely draining (trunk) rivers across our study area exhibit a consistent, distinctive pattern of higher
- 88 k_{sn} than their tributaries using a typical $\theta_{ref} = 0.5$, shown in χ -z plots (Fig. 1). As outlined above, the simplest
- interpretation of this pattern is that rivers are adjusted to spatially variable conditions (U or K), implying
- 90 trunk and tributary rivers systematically experience different conditions (e.g., average rainfall)(11). Here,
- 91 the discrepancy between trunk and tributary channel steepness is greatly reduced in χ_Q -z space using θ_{ref} =

- 92 0.5 (Fig. 1), bolstering the notion that profiles here are importantly influenced by spatially varying rainfall 93 and that k_{snO} captures this influence. Alternatively, the discrepancy between large trunk and small tributary 94 rivers may simply reflect an incorrect choice of θ_{ref} , which must be evaluated. 95 Quantitative comparisons between tributary k_{sn} or k_{snO} and equivalent trunk river segments (1694 tributarytrunk pairs) across the study area is shown in Fig. 2. This confirms that trunk k_{sn} is higher than tributaries, 96 97 on average, using a typical θ_{ref} = 0.5 and reveals greater disparities at lower elevations (Fig. 2A-C). Also, tributaries – which are more sensitive to varying environmental conditions (11, 33) – indicate a transition 98 99 between increasing and decreasing k_{sn} with outlet elevation at \sim 2 km. Although this pattern is consistent with rainfall variations (Fig. 1), spatial gradients in uplift rate cannot be discounted without first establishing 100 101 the sensitivity of k_{sn} to rainfall. 102 Alternatively, trunk and tributary k_{sn} are nearly equal on average using θ_{ref} =0.3 (Fig. 2D). If θ_{ref} = 0.3 is a 103 good description of these profiles, this finding would imply that K is approximately uniform, and that K 104 and thus k_{sn} are not strongly affected by rainfall (Figs. 2d,e). The k_{sn} -elevation pattern is not sensitive to θ_{ref} 105 (Fig. 2F), but quasi-uniform K would suggest k_{sn} variations likely reflect spatial gradients in uplift rate. 106 However, $\theta_{ref} = 0.3$ is low compared to commonly observed values (31) and further is incompatible with 107 the high concavities observed along trunk rivers in this part of the Andes (32, 41), rendering the 108 appropriateness of the "optimal" $\theta_{ref} = 0.3$ questionable. 109 In contrast, k_{snO} is predicated on the assumption that K depends strongly on climate (Eqns. 1 and 2c). The 110 relationship between trunk and tributary k_{snQ} using $\theta_{ref} = 0.5$ is indistinguishable from linear (Figs. 2g,h). 111 That variations in K expected from discharge accumulation under the observed rainfall pattern reconcile differences between trunk and tributary channel steepness implies that rivers are largely adjusted to the 112 113 rainfall pattern. This likely precludes recent substantial changes to the rainfall pattern as any such changes would force trunk and tributary k_{snQ} out of alignment. Moreover, discharge accumulation patterns have 114 115 spatial complexity unlikely to be mirrored by uplift patterns. The k_{snO} pattern is distinct from k_{sn} , suggesting quasi-uniform, high erosion rates in tributaries with outlet elevations <2 km, above which tributary 116 headwaters often tap the low-relief plateau (Fig. 1) causing catchment mean k_{snQ} to decline (Fig. 2I). 117 118 Collinearity: Along-strike Variations and Limitations We next explore the potential for along-strike variations in θ_{ref} by optimizing collinearity of all profiles 119
- within each catchment a more detailed, local analysis than the regional analysis of tributary-trunk pairs above. Optimized θ_{ref} values for χ -transformed stream networks have a central tendency of 0.25-0.3, while χ_Q -transformed networks have a bimodal distribution with a stronger mode at 0.45-0.5 and a weaker one at 0.25-0.3 (Fig. 3A). Although θ_{ref} optimizations in individual catchments are, collectively, consistent with

the regional analysis, they suggest substantial inter-catchment variability. If true, this would complicate topographic analyses and potentially confound efforts to evaluate relationships between erosion and topography (29, 37).

Notably, increasing the minimum drainage area in the channel network from 1 km² to 5 km² dramatically reduces variability in optimized θ_{ref} for χ_Q -transformed stream networks (Fig. 3B). With this trimmed stream network, a single mode at 0.45-0.5 emerges with ~70% of catchments falling within the typical 0.4-0.6 range, reinforcing the interpretation that channels are largely adjusted to the rainfall pattern. Remaining catchments outside this range have variable lithology (15, 16) and/or are small (<200–300 km²) (see Supplementary Material). Increasing this threshold further to 10 km² has little additional effect in our study basins except to increase the frequency of outliers, which reflects a trade-off where the sparsity of tributaries in the remaining stream network becomes a limiting factor (Fig. 3C). Interestingly, optimized θ_{ref} based on χ -transformed profiles are less affected. A broad mode centered at 0.3-0.35 includes most catchments but an additional mode at 0.45-0.5 appears. Catchments comprising the 0.45-0.5 mode tend to have less spatially variable rainfall (lower standard deviation). This shift toward a bimodal distribution continues as we increase the drainage area further, but outliers also become more common like we observe for χ_Q -transformed stream networks.

We suggest that the effect of increasing the minimum drainage area suggests variability of optimized θ_{ref} in the χ_Q -z analysis (Fig. 3A) largely reflects limitations imposed by the spatial resolution of the rainfall data. At 1 km², the area defining streams is much smaller than resolution of the rainfall grid (~20 km²). Consequently, rainfall estimates at small drainage areas, particularly in high-relief tributaries with associated spatial rainfall variability, are likely to be inaccurate. This can produce anomalous k_{snQ} values that can bias the results of the θ_{ref} optimization. Smaller catchments comprising fewer streams are more sensitive to anomalous values as these artifacts affect a larger fraction of the total stream network. Spatially varying tectonics and lithology can have similarly strong influences on optimized values in small catchments for this same reason. Additionally, debris flows or other processes important in high-relief terrain may compound these issues at small drainage areas (42), which may explain some changes to the "optimized" θ_{ref} values.

Erosion Rates and Topography

Metrics k_{sn} and k_{snQ} ultimately predict distinct erosion rate patterns (Figs. 2,4). At the broad scale, the k_{sn} pattern is not sensitive to θ_{ref} and predicts a more homogenous erosion pattern than k_{snQ} (Fig, 4a-c). Also, importantly, k_{sn} systematically predicts higher erosion rates than k_{snQ} at high elevations because it does not account for the rainfall pattern. Here, the 2 m/yr rainfall contour nicely separates domains where k_{sn} and

156 k_{snO} predict higher erosion rates (Fig. 4D). These observations are all consistent with the expectation that 157 many factors are convolved within k_{sn} . In contrast, to the extent that k_{snQ} captures the influence of climate, 158 it better isolates tectonic and lithologic factors (Fig. 4C,E). 159 Indeed, plotting new and published (43-46) erosion rates from quasi-steady state catchments (E=U) across 160 the study area against k_{sn} and k_{snO} reveals the potential for k_{snO} to overcome limitations of k_{sn} where climate, 161 lithology, and tectonics co-vary (Fig. 5). Further, consequences of carrying forward faulty assumptions (e.g., quasi-uniform K despite variable lithology and rainfall) during topographic analyses are evident. It is 162 163 difficult to detect any consistent relationships among k_{sn} , erosion rate, lithology, and climate for catchments in the Eastern Cordillera (EC), particularly for θ_{ref} = 0.3, and only pronounced lithologic contrasts between 164 165 EC and Subandean catchments are apparent (Figs. 5a,b). This could be mistakenly interpreted to suggest the influences from climate in general and lithologic variations in the EC are weak or absent. In contrast, 166 167 k_{snQ} resolves distinct relationships separated by 3-fold differences in K_p between resistant (quartzite-rich) metasedimentary rocks and plutonic/weaker metamorphic rocks comprising EC catchments (Fig. 5C). 168 169 Clustering, particularly of catchments with plutonic bedrock, that experience disparate rainfall but have 170 similar k_{snO} further supports the interpretation that k_{snO} is capturing the influence of climate. As transient responses to recent changes to the rainfall pattern would tend to disrupt such clustering (11), this 171 observation also bolsters the interpretation that catchments reflect quasi-adjustment to the modern rainfall 172 173 pattern. 174 This example highlights the need for caution, however, when considering relationships between erosion rates and k_{snO} , particularly where strong variations in rainfall are present. Because k_{snO} magnifies differences 175 between catchments with different lithology that also experience different amounts of rainfall, it is better 176 177 able to resolve distinct lithologic trends. However, failure to segregate samples populating these different 178 trends would increase data scattering and result in apparently weaker correlations. Catchments containing 179 more than one lithology are also likely to plot in intermediate positions between distinct endmembers, 180 which can compound apparent scatter and potentially distort endmember trends. 181 Interestingly, we also find that k_{snQ} also implies that topography is more sensitive to uplift rate than k_{sn} , 182 reflected by lower values for power-law exponent n (Eqn. 2)(2). While we emphasize that a range of n183 values (and associated erosional efficiency coefficients) can fit these data reasonably well, relationships 184 determined using k_{snQ} are better constrained than k_{sn} (see Supplementary Material). This apparently weaker topographic sensitivity to uplift rate (higher n) and weaker constraints on this sensitivity (range of 185 compatible n values) are both attributable to mixing of lithologic and climatic influences in k_{SN} . 186 187 Additionally, after accounting for rainfall variations with k_{snQ} we do not resolve any dependence of n on 188 climate, consistent with results from the Himalaya (1, 19). This may reflect continuity of quasi-linear

scaling between threshold-exceeding flood discharges and MAP across climate regimes in our study (1, 12). We expect any climate-dependent departures from this scaling would inhibit data collapse using similar n values, particularly among catchments with disparate rainfall. Notably, variable n values with climate and breakdown of quasi-linear scaling should also be expressed in collinearity between trunk and tributary rivers, which we do not observe (Fig. 2G). Together, these findings suggest capturing the influence of climate is an important precondition to understanding interactions among topography, erosion, and other environmental variables.

Implications for Landscape Analysis

189

190

191

192

193194

195

196

197

198

199 200

201

202

203

204

205

206207

208

209210

211

212

213

214

215

216

217

218219

This analysis reveals important considerations for future landscape analyses. Although we argue that tributaries here have lower k_{sn} than trunk rivers due to climate-driven variations in erosional efficiency (K), anytime large and small rivers exhibit this pattern a lower θ_{ref} will decrease the channel steepness disparity between them. Optimizing collinearity between rivers in χ -z space will return the θ_{ref} value that best approximates assumptions required for equal k_{sn} : spatially uniform K and U. Under such conditions, differences in slope are directly related to differences in upstream drainage area. In practice, enforcing this condition optimizes convolution of any environmental variations that exist with drainage area, and systematic spatial gradients in K and/or U will bias optimized values. This of course is problematic if the goal is to extract meaningful information about controls on channel steepness. Further, rather than true variability in θ_{ref} , variability in optimized values likely reflects spatially variable K and/or U (i.e., violations of collinearity requirements, not variations in factors controlling intrinsic profile concavity represented by m/n in the SPM). This same reasoning applies to k_{snO} . However, unlike k_{sn} where orographic rainfall can systematically affect K between catchments across large areas and effects of these rainfall variations can propagate downstream (e.g., integrating dry headwaters)(11), lithology ($\sim K_p$) and data resolution limitations primarily affect k_{snQ} only locally. Collinearity optimization algorithms are better-equipped to handle localized perturbations (36), decreasing potential for biased θ_{ref} estimates based on χ_Q -z collinearity.

Despite these strengths, we do not necessarily expect all landscapes are in quasi-equilibrium with modern MAP. These exceptions may reflect important complexities of the local hydroclimate or recent climate changes that have substantially altered modern rainfall patterns (e.g., refs(47–49)). Also, spatial gradients in uplift can differently influence trunk and tributary k_{snQ} . In all these cases, optimizing χ_Q -z collinearity may also give biased θ_{ref} estimates, the use of which may complicate k_{snQ} -erosion rate relationships and distort the apparent influence of different environmental variables. As such, we caution that these factors should considered when interpreting χ_Q -z collinearity.

We conclude that k_{snQ} based on MAP with $\theta_{ref} \approx 0.45$ -0.5 provides the best remote estimate of spatial variations in erosion at the landscape sale. Calibrated with erosion rate measurements it can dramatically improve understanding of primary environmental controls on landscape evolution. These findings are unaffected by the diverse climatic, tectonic, and morphologic conditions across >1500 km along strike on the eastern flank of the central Andes, demonstrating that climate exerts a strong, ubiquitous influence on erosional efficiency and topography.

MATERIALS AND METHODS

227 Topographic Analysis

We use one-arcsecond (\sim 30 m) Shuttle Radar Topography Mission digital elevation model (50) and TRMM-2B31 (Tropical Rainfall Measuring Mission) rainfall data (51), which has \sim 4.5 km horizontal resolution at this latitude. We extracted and analyzed river profiles from 104 transversely draining catchments (> 100 km 2) that span >1500 km north-to-south along the eastern margin of the northern-central Andes using built-in functions in TopoToolbox and the Topographic Analysis Kit (52, 53). We extract the longest (trunk) river from each of the 104 transverse catchments and all tributaries that drain directly into the trunk stream with drainage area between 5 and 100 km 2 (1694 total). Then we apply the χ -transform (34) to stream networks to linearize profiles in χ -elevation plots:

$$\chi = \int_{x_b}^{x} \left(\frac{A_0}{A(x)}\right)^{\theta_{ref}} dx,\tag{3a}$$

$$z(x) = z(x_h) + k_{sn} \cdot \gamma, \tag{3b}$$

where x is distance upstream; x_b is the outlet position; A_0 is a reference drainage area, here set equal to 1 km²; and z is elevation. The above equations can similarly be cast in terms of discharge (Q) rather than drainage area to arrive at χ_Q and k_{snQ} (11, 40):

$$\chi_Q = \int_{x_b}^x \left(\frac{Q_0}{Q(x)}\right)^{\theta_{ref}} dx,\tag{4a}$$

$$z(x) = z(x_h) + k_{sn0} \cdot \chi_0. \tag{4b}$$

Collinearity is defined as the degree to which two river segments collapse to a single line in χ -z (or χ_Q -z), which we quantify in two ways. The first method directly compares average channel steepness (k_{sn} and k_{snQ}) of tributaries with equivalent segments of its trunk river: lines may only be collinear if they have equal slopes. We calculate average channel steepness for each tributary as its fluvial relief divided by the change in χ (or χ_Q), both of which are measured from the tributary confluence with the trunk river upstream to a minimum drainage area of 1 km² (i.e., $k_{sn} = \Delta z/\Delta \chi$). Average k_{sn} and k_{snQ} for comparable segments of the

trunk river are calculated using $\Delta \chi$ (or $\Delta \chi_Q$) along the trunk river over the same elevation range as for each tributary. Results and interpretations are not sensitive to different methods of calculating average k_{sn} or k_{snQ} , for example with a fixed segment smoothing distance.

The second method optimizes θ_{ref} values for both for k_{sn} and k_{snQ} that maximize collinearity in χ -z and χ_Q -z, respectively, in individual catchments using the 'mnoptimvar' function in TopoToolbox (52) (c.f.,(36, 39)). It operates by segmenting stream networks from each catchment into bins of equal χ (or χ_Q). The function then searches for the θ_{ref} value that minimizes elevation differences as quantified by a user-defined variability statistic among stream segments across all bins. Optimization results presented in the main text use the 'robustcov' function in MATLAB, which implements an efficient algorithm to estimate the minimum covariance determinant (54). Minimizing interquartile range and standard deviation yield comparable results. Results do not appear sensitive to the number of bins or to the minimum number of stream segments within each bin. As discussed in the main text, optimized values reflect those that best align with assumptions for collinearity, which are not necessarily equivalent to the most appropriate θ_{ref} value, particularly in catchments with spatially varying environmental factors (Supplementary Material).

Interpolated maps for k_{sn} and k_{snQ} are all generated from the same stream network. Color ramps for k_{sn} and k_{snQ} maps are normalized to reflect equivalent data ranges that include ~99.5% of pixel values. This range was determined to exclude outliers that saturate color maps. The normalized difference map was calculated by first normalizing values in k_{sn} and k_{snQ} maps between 0 and 1. Color ramp was then optimized for visualization centered on a value of 0 with symmetrical ranges above and below.

¹⁰Be Sample Preparation

Southern Peru samples were collected in 2018 from active channel deposits of quasi-steady state trunk-stream tributaries, and processes at the WOMBAT laboratory at the School of Earth and Space Exploration at Arizona State University. Samples were first rinsed and dry-sieved to yield 250-1000 µm fraction. Sieved samples were cleaned using a 2:1 solution of hydrochloric acid (HCl) and nitric acid (HNO₃). Samples underwent density separation using lithium polytungstate (LST) to remove heavy minerals, which was then diluted to separate quartz from less dense minerals. Samples were leached using 1-2% hydrofluoric acid (HF) and HNO₃ solution and rolled on heat for 6-8 hours. Samples underwent a minimum of 10 leaches to eliminate mineral species other than quartz and ensure complete etching of quartz grains. Once quartz fractions were purified, samples were spiked with a commercial ⁹Be solution and dissolved in HF and HNO₃. Beryllium was extracted through standard anion and cation chromatography techniques, oxidized in a muffle furnace, and mixed with a niobium matrix and loaded into cathodes for analysis on the

accelerator mass spectrometer at Purdue Rare Isotope Measurement Laboratory. Reported ¹⁰Be/⁹Be ratios are blank corrected.

Erosion Rate Calculation, Curation, and Regression Analysis

Published erosion rates were recalculated using a common workflow to ensure robust comparisons and curated to exclude catchments unlikely to reflect quasi-steady state conditions. We exclude catchments with large slope-break knickpoints, which unfortunately includes a considerable fraction of catchments from the various published datasets. Overwhelmingly, remaining catchments are composed of a single lithology (*15*, *16*), and those comprising more than one lithology are classified according to the dominant lithology by extent within the catchment. Channel steepness for new and published samples in quasi-steady state catchments were calculated with a minimum drainage area of 1 km² and 500 m smoothing distances. Erosion rates were recalculated using a production-rate weighted elevation following procedures of Portenga and Bierman (*55*) and published ¹⁰Be concentrations were scaled to all be consistent with 07KNSTD standard (*56*). Erosion rates were then calculated using the CRONUS online calculator (version 3.0)(*57*, *58*). We assume no topographic shielding, 0 cm sediment thickness, and density of 2.65 g/cm³, and use the 'std' elevation flag. Erosion rates are calculated using time-invariant production rate scaling (*59*), and are quoted with 1σ external uncertainty.

Regressions analysis was conducted following methods from Adams et al.(I). Quality of fits was evaluated using the MSWD, which can account for uncertainties on individual measurements in both x and y directions. Well fit models should approach $1 \pm 2\sigma$, with higher values indicating that data are over-dispersed and the degree to which uncertainties are likely underestimated (60). Models are fit using 2σ external uncertainties on erosion rate measurements and 2 SE on k_{sn} and k_{snQ} . We fit distinct relationships apparent in k_{sn} -E and k_{snQ} -E in two ways using the 'MC York' MATLAB function from Adams et al.(I). In the first, we allow both the power-law coefficient (K or K_p) and exponent (I) vary freely to arrive at the best-fit pair of parameter values. In the second, we fix I to find the best-fit I0 or I1 or I2 or I3 advantage to fixing the I3 exponent allows for direct comparison of I3 or I4 values between trends and is therefore preferred. Five samples with Neogene-Paleogene age bedrock from Hippe et al.(I3) were excluded from all fitting because they do not correlate with rocks of similar age across the study area, unlike other rock units, and were not fit separately due to their small population and narrow ranges of both channel steepness and erosion rate.

ACKNOWLEDGMENTS

- 311 This paper benefitted from insightful comments and reviews from Bodo Bookhagen, an anonymous
- 312 reviewer, and Associate Editor Darryl Granger. We thank Víctor Carlotto (Universidad Nacional San
- Antonio Abad del Cusco) for assistance with field work. Funding: this research was supported by the
- National Science Foundation (EAR-1842065 to K.X.W.). Data and Materials Availability: All data
- needed to evaluate the conclusions in the paper are present in the paper and/or the Supplementary Materials.
- 316 **Author Contributions:** J.S.L and K.X.W performed field work and data analysis. Laboratory analyses
- 317 were carried out by J.S.L. A.M.H. provided lab facilities and assistance. All authors commented on and
- 318 contributed to the final manuscript. **Competing Interests:** The authors declare that they have no competing
- 319 interests.

320 REFERENCES

- 321 1. B. A. Adams, K. X. Whipple, A. M. Forte, A. M. Heimsath, K. V. Hodges, Climate controls on
- erosion in tectonically active landscapes. *Sci. Adv.* **6**, eaaz3166 (2020).
- 2. D. Lague, The stream power river incision model: Evidence, theory and beyond. *Earth Surf.*
- 324 *Process. Landforms.* **39**, 38–61 (2014).
- 325 3. K. X. Whipple, R. A. DiBiase, B. T. Crosby, *Bedrock Rivers* (Elsevier Ltd., 2013;
- 326 http://dx.doi.org/10.1016/B978-0-12-374739-6.00254-2), vol. 9.
- 4. D. W. Burbank, A. E. Blythe, J. Putkonen, B. Pratt-Sitaula, E. Gabet, M. Oskin, A. Barros, T. P.
- Ojha, Decoupling of erosion and precipitation in the Himalayas. *Nature.* **426**, 652–655 (2003).
- 329 5. V. Godard, D. L. Bourlès, F. Spinabella, D. W. Burbank, B. Bookhagen, G. B. Fisher, A. Moulin,
- L. Léanni, Dominance of tectonics over climate in himalayan denudation. *Geology.* **42**, 243–246
- 331 (2014).
- 332 6. H. Seybold, W. R. Berghuijs, J. P. Prancevic, J. W. Kirchner, Global dominance of tectonics over
- climate in shaping river longitudinal profiles. *Nat. Geosci.* **14**, 503–507 (2021).
- 7. D. R. Montgomery, G. Balco, S. D. Willett, Climate, tectonics, and the morphology of the Andes.
- 335 *Geology.* **29**, 579–582 (2001).
- 336 8. S. A. Chen, K. Michaelides, S. W. D. Grieve, M. B. Singer, Aridity is expressed in river
- 337 topography globally. *Nature*. **573**, 573–577 (2019).
- 338 9. D. P. Finlayson, D. R. Montgomery, B. Hallet, Spatial coincidence of rapid inferred erosion with
- young metamorphic massifs in the Himalayas. *Geology*. **30**, 219–222 (2002).

- 340 10. B. Bookhagen, M. R. Strecker, Spatiotemporal trends in erosion rates across a pronounced rainfall
- gradient: Examples from the southern Central Andes. Earth Planet. Sci. Lett. 327–328, 97–110
- 342 (2012).
- 343 11. J. S. Leonard, K. X. Whipple, Influence of Spatial Rainfall Gradients on River Longitudinal
- Profiles and the Topographic Expression of Spatially and Temporally Variable Climates in
- 345 Mountain Landscapes. J. Geophys. Res. Earth Surf. 126 (2021), doi:10.1029/2021JF006183.
- 346 12. M. W. Rossi, K. X. Whipple, E. R. Vivoni, Precipitation and evapotranspiration controls on daily
- runoff variability in the contiguous United States and Puerto Rico. J. Geophys. Res. Earth Surf.
- **121**, 128–145 (2016).
- 349 13. B. K. Horton, Sedimentary record of Andean mountain building. *Earth-Science Rev.* 178, 279–309
- 350 (2018).
- 351 14. B. T. Bishop, S. L. Beck, G. Zandt, L. Wagner, M. Long, S. K. Antonijevic, A. Kumar, H. Tavera,
- Causes and consequences of flat-slab subduction in southern Peru. *Geosphere*. **13**, 1392–1407
- 353 (2017).
- 15. INGEMMET, "Geological Map of Peru (1:1,000,000)" (Intituto Geologico, Minero Y
- 355 Metalurgico, Lima, 2016).
- 356 16. SERGEOMIN, "Mapa Geologico de Bolivia 1:1,000,000" (La Paz, 2001).
- 357 17. K. X. Whipple, R. A. DiBiase, B. Crosby, J. P. L. Johnson, *Bedrock Rivers* (Elsevier, Second Edi.,
- 358 2022; http://dx.doi.org/10.1016/B978-0-12-818234-5.00101-2), vol. 6.
- 359 18. P. Molnar, R. S. Anderson, G. Kier, J. Rose, Relationships among probability distributions of
- stream discharges in floods, climate, bed load transport, and river incision. J. Geophys. Res. Earth
- 361 *Surf.* **111**, 1–10 (2006).
- 362 19. D. Scherler, R. A. DiBiase, G. B. Fisher, J. P. Avouac, Testing monsoonal controls on bedrock
- river incision in the Himalaya and Eastern Tibet with a stochastic-threshold stream power model.
- *J. Geophys. Res. Earth Surf.* **122**, 1389–1429 (2017).
- 365 20. A. M. Forte, J. S. Leonard, M. W. Rossi, K. X. Whipple, A. M. Heimsath, L. Sukhishvili, T.
- Godoladze, F. Kardirov, Low variability, snowmelt runoff inhibits coupling of climate, tectonics
- and topography in the Greater Caucasus. *Earth Planet. Sci. Lett.* **584**, 68–70 (2022).
- 368 21. E. Deal, J. Braun, G. Botter, Understanding the Role of Rainfall and Hydrology in Determining

- Fluvial Erosion Efficiency. J. Geophys. Res. Earth Surf. 123, 744–778 (2018).
- 370 22. G. E. Tucker, Drainage basin sensitivity to tectonic and climatic forcing: Implications of a
- 371 stochastic model for the role of entrainment and erosion thresholds. *Earth Surf. Process*.
- 372 *Landforms.* **29**, 185–205 (2004).
- 373 23. D. Lague, N. Hovius, P. Davy, Discharge, discharge variability, and the bedrock channel profile.
- 374 *J. Geophys. Res. Earth Surf.* **110**, 1–17 (2005).
- 375 24. J. Han, N. M. Gasparini, J. P. L. Johnson, B. P. Murphy, Modeling the influence of rainfall
- gradients on discharge, bedrock erodibility, and river profile evolution, with application to the Big
- 377 Island, Hawai'i. *J. Geophys. Res. Earth Surf.* **119**, 1418–1440 (2014).
- 378 25. C. M. Shobe, G. E. Tucker, M. W. Rossi, Variable-Threshold Behavior in Rivers Arising From
- 379 Hillslope-Derived Blocks. *J. Geophys. Res. Earth Surf.* **123**, 1931–1957 (2018).
- 380 26. B. P. Murphy, J. P. L. Johnson, N. M. Gasparini, L. S. Sklar, Chemical weathering as a
- mechanism for the climatic control of bedrock river incision. *Nature*. **532**, 223–227 (2016).
- 382 27. S. M. Olen, B. Bookhagen, M. R. Strecker, Role of climate and vegetation density in modulating
- denudation rates in the Himalaya. *Earth Planet. Sci. Lett.* **445**, 57–67 (2016).
- 384 28. M. A. Harel, S. M. Mudd, M. Attal, Global analysis of the stream power law parameters based on
- worldwide 10Be denudation rates. *Geomorphology*. **268**, 184–196 (2016).
- 386 29. C. Wobus, K. X. Whipple, E. Kirby, N. Snyder, J. Johnson, K. Spyropolou, B. Crosby, D.
- 387 Sheehan, Tectonics from topography: Procedures, promise, and pitfalls. Spec. Pap. Geol. Soc. Am.
- **398**, 55–74 (2006).
- 389 30. G. E. Tucker, K. X. Whipple, Topographic outcomes predicted by stream erosion models:
- Sensitivity analysis and intermodel comparison. J. Geophys. Res. Solid Earth. 107, 1-16 (2002),
- 391 doi:10.1029/2001JB000162.
- 392 31. E. Kirby, K. X. Whipple, Expression of active tectonics in erosional landscapes. *J. Struct. Geol.*
- **44**, 54–75 (2012).
- 394 32. N. M. Gasparini, K. X. Whipple, Diagnosing climatic and tectonic controls on topography: Eastern
- flank of the northern Bolivian Andes. *Lithosphere*. **6**, 230–250 (2014).
- 33. J. Han, N. M. Gasparini, J. P. L. Johnson, Measuring the imprint of orographic rainfall gradients
- on the morphology of steady-state numerical fluvial landscapes. *Earth Surf. Process. Landforms*.

- **40**, 1334–1350 (2015).
- 399 34. J. T. Perron, L. Royden, An integral approach to bedrock river profile analysis. *Earth Surf.*
- 400 *Process. Landforms.* **38**, 570–576 (2013).
- 401 35. G. H. Roe, D. R. Montgomery, B. Hallet, Effects of orographic precipitation variations on the
- 402 concavity of steady-state river profiles. *Geology*. **30**, 143–146 (2002).
- 403 36. S. M. Mudd, F. J. Clubb, B. Gailleton, M. D. Hurst, How concave are river channels? *Earth Surf.*
- 404 *Dyn.* **6**, 505–523 (2018).
- 405 37. B. Gailleton, S. M. Mudd, F. J. Clubb, S. W. D. Grieve, M. D. Hurst, Impact of Changing
- 406 Concavity Indices on Channel Steepness and Divide Migration Metrics. J. Geophys. Res. Earth
- 407 Surf. **126** (2021), doi:10.1029/2020jf006060.
- 408 38. L. Goren, M. Fox, S. D. Willett, Tectonics from fluvial topography using formal linear inversion:
- Theory and applications to the Inyo Mountains, California. J. Geophys. Res. F Earth Surf. 119,
- 410 1651–1681 (2014).
- 411 39. S. Hergarten, J. Robl, K. Stuwe, Tectonic geomorphology at small catchment sizes-extensions of
- 412 the stream-power approachand the x method. *Earth Surf. Dyn.* **4**, 1–9 (2016).
- 413 40. R. Yang, S. D. Willett, L. Goren, In situ low-relief landscape formation as a result of river network
- 414 disruption. *Nature*. **520**, 526–529 (2015).
- 415 41. K. Norton, F. Schlunegger, Migrating deformation in the Central Andes from enhanced orographic
- 416 rainfall. Nat. Commun. 2 (2011), doi:10.1038/ncomms1590.
- 417 42. J. Stock, W. E. Dietrich, Valley incision by debris flows: Evidence of a topographic signature.
- 418 Water Resour. Res. 39 (2003), doi:10.1029/2001WR001057.
- 419 43. E. B. Safran, P. R. Bierman, R. Aalto, T. Dunne, K. X. Whipple, M. Caffee, Erosion rates driven
- by channel network incision in the Bolivian Andes. *Earth Surf. Process. Landforms.* **30**, 1007–
- 421 1024 (2005).
- 422 44. N. Insel, T. A. Ehlers, M. Schaller, J. B. Barnes, S. Tawackoli, C. J. Poulsen, Spatial and temporal
- 423 variability in denudation across the Bolivian Andes from multiple geochronometers.
- 424 *Geomorphology.* **122**, 65–77 (2010).
- 425 45. K. Hippe, F. Kober, G. Zeilinger, S. Ivy-Ochs, C. Maden, L. Wacker, P. W. Kubik, R. Wieler,
- Quantifying denudation rates and sediment storage on the eastern Altiplano, Bolivia, using

- 427 cosmogenic 10Be, 26Al, and in situ 14C. Geomorphology. 179, 58–70 (2012).
- 428 46. F. Kober, G. Zeilinger, K. Hippe, O. Marc, T. Lendzioch, R. Grischott, M. Christl, P. W. Kubik,
- 429 R. Zola, Tectonic and lithological controls on denudation rates in the central Bolivian Andes.
- 430 *Tectonophysics.* **657**, 230–244 (2015).
- 431 47. J. Galewsky, C. P. Stark, S. Dadson, C. C. Wu, A. H. Sobel, M. J. Horng, Tropical cyclone
- triggering of sediment discharge in Taiwan. J. Geophys. Res. Earth Surf. 111, 1–16 (2006).
- 433 48. S. J. Dadson, N. Hovius, H. Chen, W. B. Dade, M. L. Hsieh, S. D. Willett, J. C. Hu, M. J. Horng,
- M. C. Chen, C. P. Stark, D. Lague, J. C. Lin, Links between erosion, runoff variability and
- seismicity in the Taiwan orogen. *Nature*. **426**, 648–651 (2003).
- 436 49. E. Gayer, L. Michon, P. Louvat, J. Gaillardet, Storm-induced precipitation variability control of
- 437 long-term erosion. *Earth Planet. Sci. Lett.* **517**, 61–70 (2019).
- 438 50. T. G. Farr, P. A. Rosen, E. Caro, R. Crippen, R. Duren, S. Hensley, M. Kobrick, M. Paller, E.
- Rodriguez, L. Roth, D. Seal, S. Shaffer, J. Shimada, J. Umland, M. Werner, M. Oskin, D.
- Burbank, D. Alsdorf, The Shuttle Radar Topography Mission. *Rev. Geophys.* **45**, RG2004 (2007).
- 441 51. B. Bookhagen, M. R. Strecker, Orographic barriers, high-resolution TRMM rainfall, and relief
- variations along the eastern Andes. *Geophys. Res. Lett.* **35**, 1–6 (2008).
- 443 52. W. Schwanghart, D. Scherler, Short Communication: TopoToolbox 2 MATLAB-based software
- for topographic analysis and modeling in Earth surface sciences. *Earth Surf. Dyn.* **2**, 1–7 (2014).
- 445 53. A. M. Forte, K. X. Whipple, Short communication: The Topographic Analysis Kit (TAK) for
- 446 TopoToolbox. Earth Surf. Dyn. 7, 87–95 (2019).
- 447 54. P. J. Rousseeuw, K. Van Driessen, A fast algorithm for the minimum covariance determinant
- estimator. *Technometrics*. **41**, 212–223 (1999).
- 449 55. E. W. Portenga, P. R. Bierman, Understanding earth's eroding surface with 10Be. GSA Today. 21,
- 450 4–10 (2011).
- 451 56. A. T. Codilean, H. Munack, T. J. Cohen, W. M. Saktura, A. Gray, S. M. Mudd, OCTOPUS: An
- open cosmogenic isotope and luminescence database. Earth Syst. Sci. Data. 10, 2123–2139
- 453 (2018).
- 454 57. G. Balco, J. O. Stone, N. A. Lifton, T. J. Dunai, A complete and easily accessible means of
- 455 calculating surface exposure ages or erosion rates from 10Be and 26Al measurements. *Quat.*

456		Geochronol. 3, 174–195 (2008).
457 458	58.	S. M. Marrero, F. M. Phillips, B. Borchers, N. Lifton, R. Aumer, G. Balco, Cosmogenic nuclide systematics and the CRONUScalc program. <i>Quat. Geochronol.</i> 31 , 160–187 (2016).
459 460	59.	J. O. Stone, Air pressure and cosmogenic isotope production. <i>J. Geophys. Res. Solid Earth.</i> 105 , 23753–23759 (2000).
461 462	60.	I. Wendt, C. Carl, The statistical distribution of the mean squared weighted deviation. <i>Chem. Geol. Isot. Geosci. Sect.</i> 86 , 275–285 (1991).
463		
464		

465 Figures

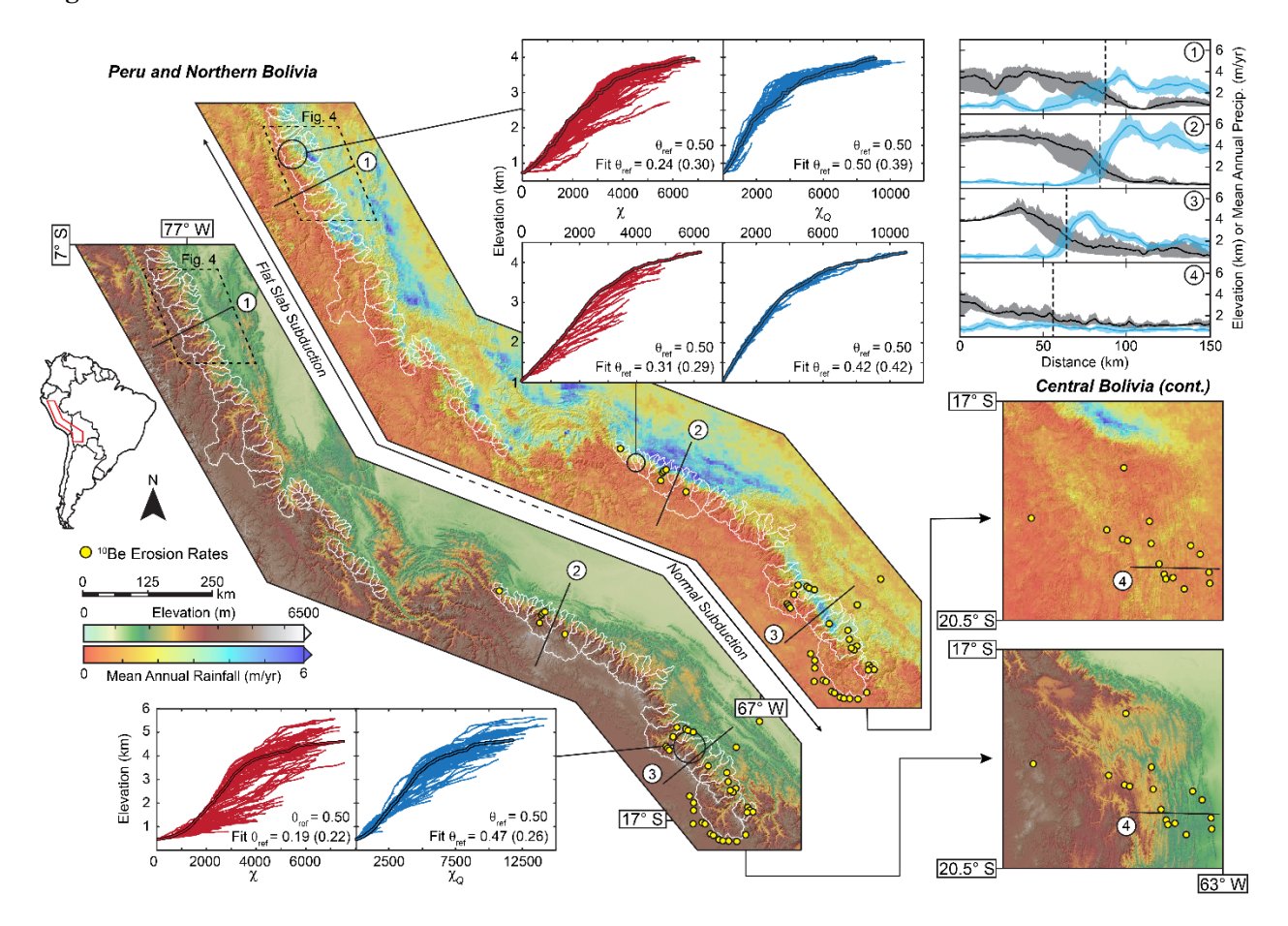


Figure 1. Map synthesizing topography, rainfall, subduction regime, and channel steepness patterns from the north-central Andes of Peru and Bolivia. Topographic analysis based on catchments outlined in white. Locations of 10 Be erosion rate measurements used for this study shown with yellow circles (54 total). Comparisons between χ -z (red), and χ_Q -z (blue) profiles for representative catchments along-strike. Trunk profiles are highlighted in black. All panels plotted with θ_{ref} = 0.5 and show optimized θ_{ref} values determined using stream networks with minimum upstream drainage area of 5 km² (and 1 km²) – see text for details. Numbered lines 1-4 on maps show centerline locations of 50 km wide swath profiles of topography and rainfall, depicted top-right. Swaths show mean, minimum, and maximum values; vertical dashed lines show position where mean elevation reaches 2 km – see text for details.

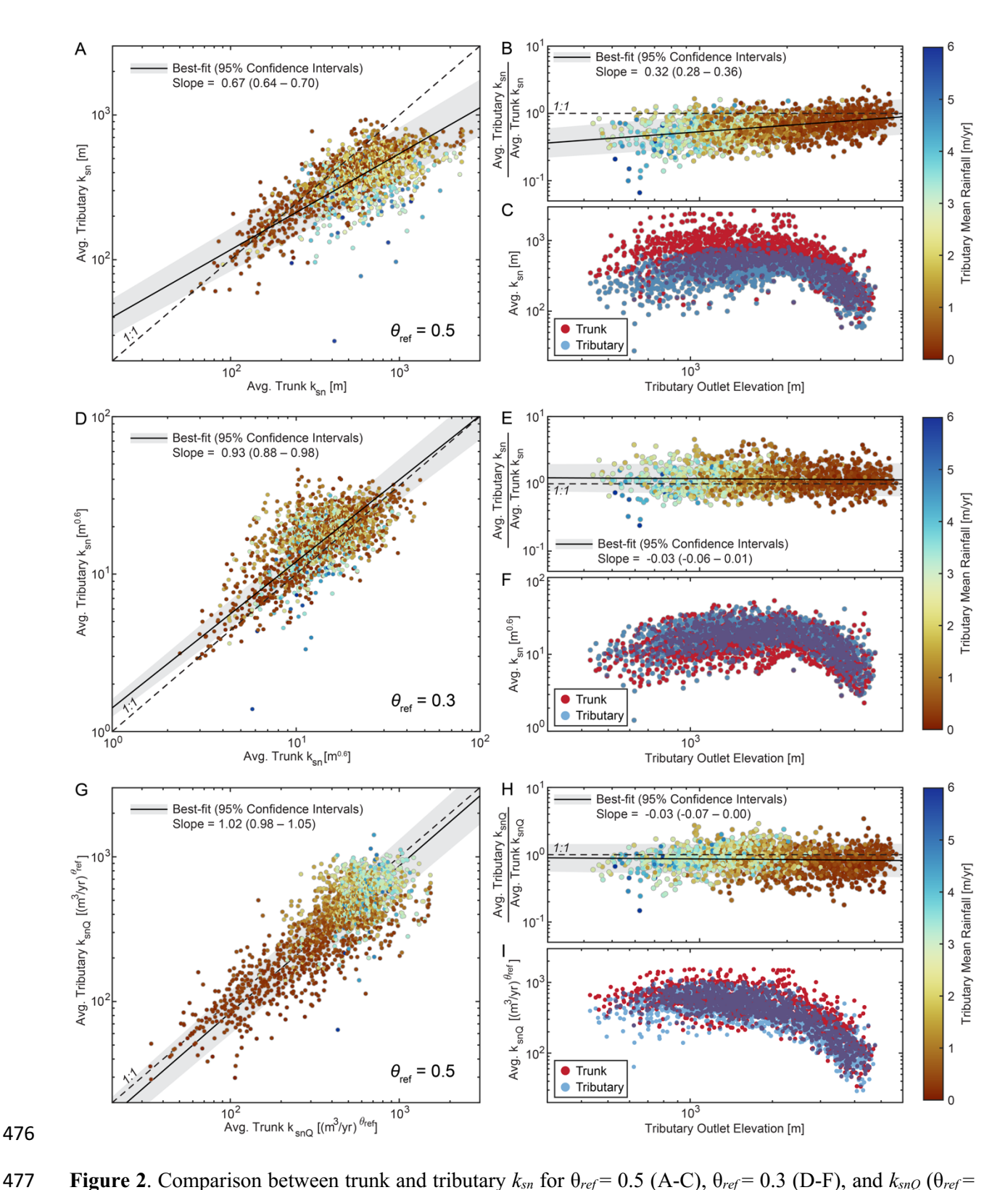


Figure 2. Comparison between trunk and tributary k_{sn} for $\theta_{ref} = 0.5$ (A-C), $\theta_{ref} = 0.3$ (D-F), and k_{snQ} ($\theta_{ref} = 0.5$; G-I). Dashed lines show 1:1 relationship. Solid black lines show total least-squares (A, D, G) and

ordinary-least-squares (B, E, H) regressions with 95% confidence intervals in gray. Spatial pattern of erosion predicted by trunk and tributary rivers shown in C,F, and I.

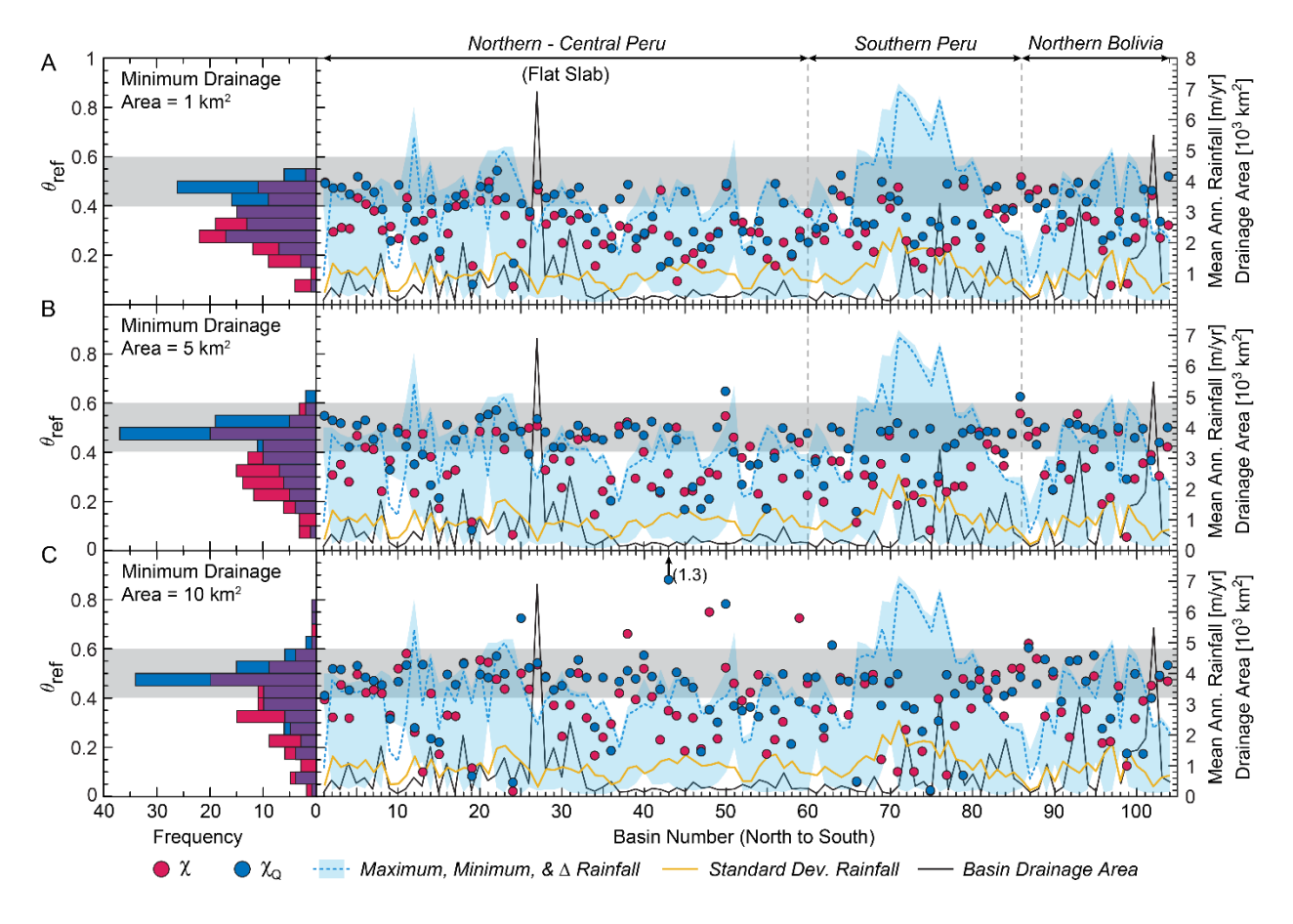


Figure 3. Analysis of optimized θ_{ref} values individually fit to χ-z profiles (red) and χ_Q -z (blue) for each catchment along-strike, and comparison between stream networks calculated with minimum drainage areas of 1 km² (A), 5km² (B), and 10km² (C). Optimized θ_{ref} values are plotted alongside catchment rainfall characteristics and drainage area. Histogram shows frequency of optimized values – see Materials and Methods and Supplementary Material.

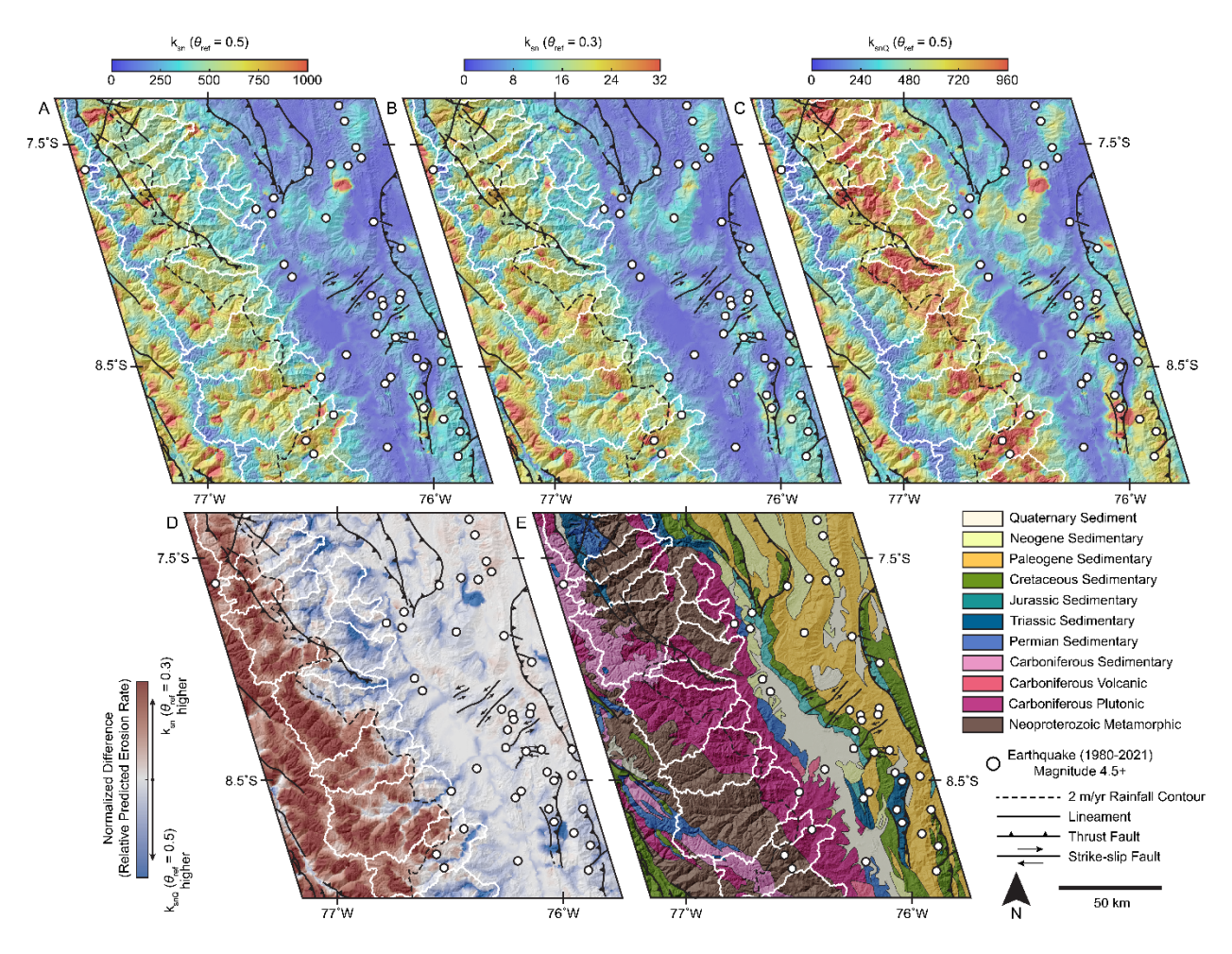


Figure 4. Comparison between interpolated maps – see Materials and Methods – of k_{sn} and k_{snQ} illustrating distinct erosion rate patterns predicted by each (A-C), difference map highlighting contrasts between k_{sn} and k_{snQ} (D) and simplified geologic map (E). Color stretches for panels (A-C) are linear minimum-maximum scales cropped to the same data range to be directly comparable while excluding outliers (colors show lower ~99.5% of the full data ranges). Geology and faults simplified from ref.(15) and recent seismicity is from the USGS earthquake catalog.

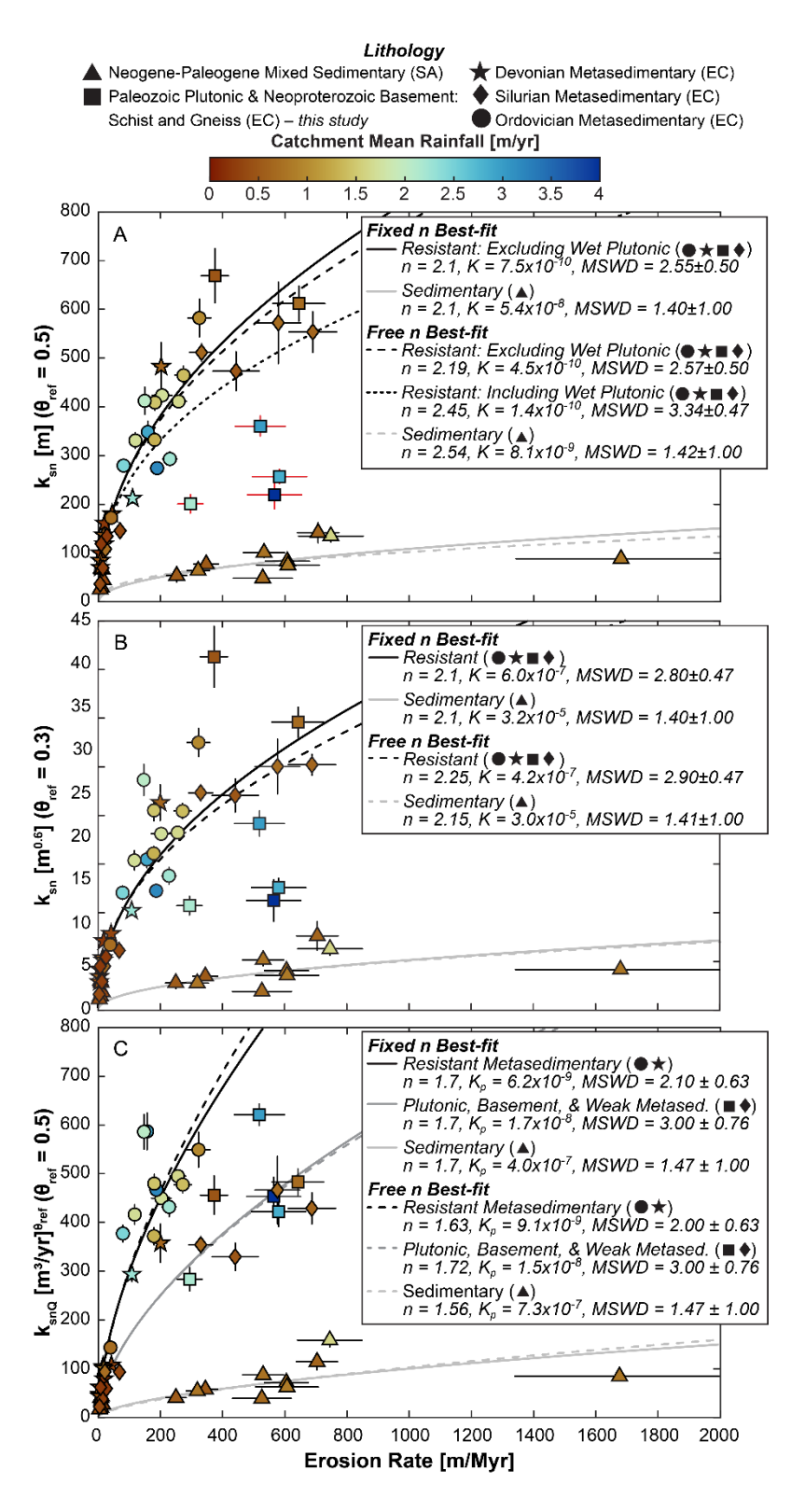


Figure 5. Synthesis of ¹⁰Be catchment-average erosion rates (54 total) from the eastern flank and of northern-central Andes, including curated published data from northern and central Bolivia (43–46) and six new rates from southern Peru. EC and SA denote association with the Eastern Cordillera and Subandes,

Manuscript submitted to Science Advances

respectively. Measurements shown with 1σ uncertainty. See Materials and Methods for details about data
curation, lithologic classification, and regression analysis. Regressions based on the best-fit fixed n values
are preferred because they allow direct comparison of K (or K_p) values between trends; results from
regressions where both n and K (or K_p) values are allowed to vary are similar and shown for comparison.
Samples from catchments with Plutonic bedrock and high rainfall (Wet Plutonic) excluded from fitting in
(A) are shown with red error bars; however, these samples are not excluded from fitting in (B) because $\theta_{\textit{ref}}$
= 0.3 here implies K is independent from rainfall. Note, k_{snQ} resolves distinct trends among resistant rock
types found in the EC that are not evident using k_{sn} , and best-fit n values for k_{sn} (both θ_{ref}) are higher than
for k_{snQ} . Further, note clustering of plutonic bedrock samples (squares) experiencing wide variations in
rainfall in (C) compared with scattering exhibited by these same sample in (A) and (B).



Isolating climatic, tectonic, and lithologic controls on mountain landscape evolution

Joel S. Leonard^{1*}, Kelin X. Whipple¹, and Arjun M. Heimsath¹

School of Earth and Space Exploration, Arizona State University, Tempe, Arizona, USA

*Corresponding author. Email: joel.leonard@asu.edu

This PDF file includes:

Figs. S1 to S2

Other Supplementary Materials for this manuscript include the following:

Data S1

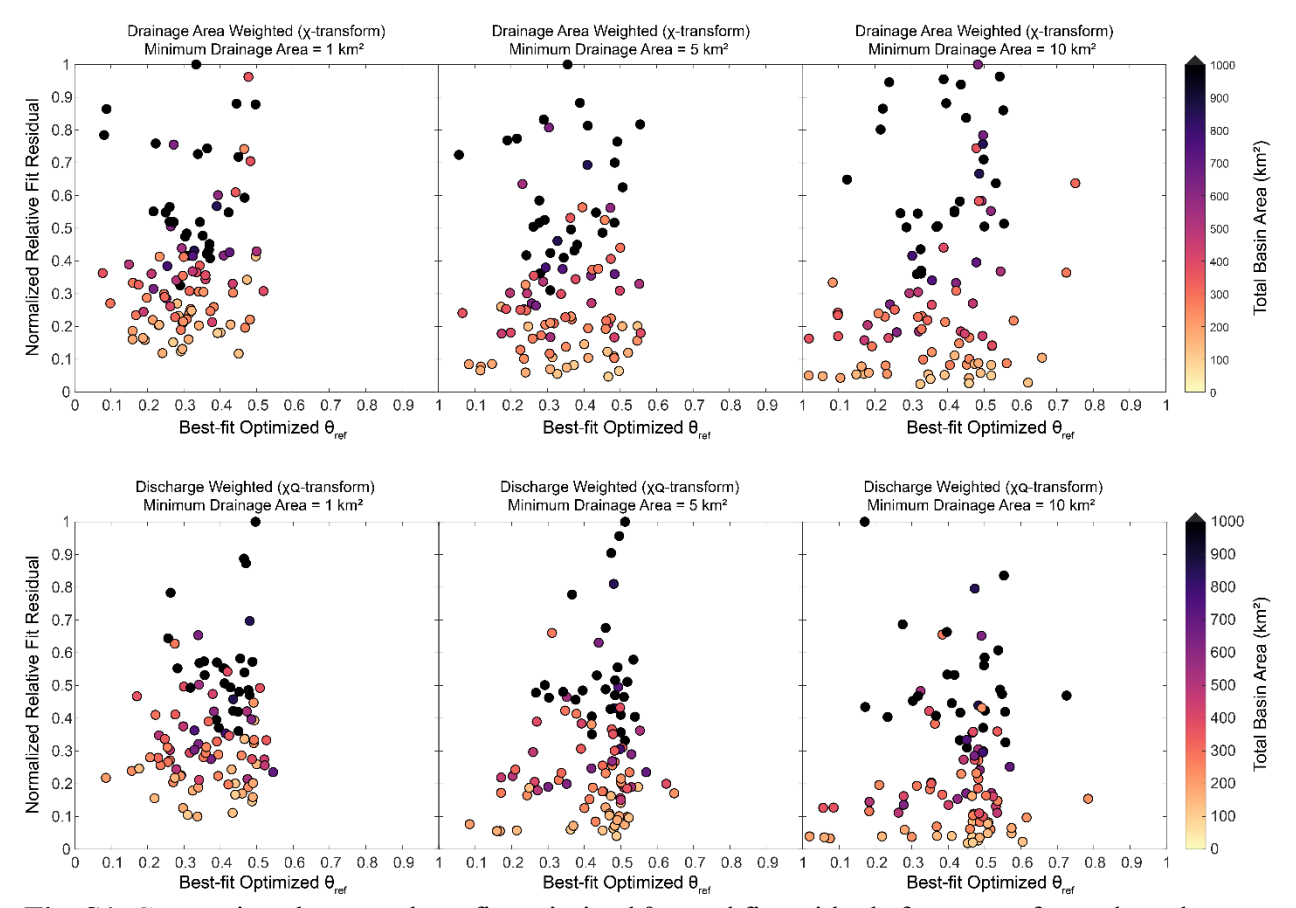


Fig. S1. Comparison between best-fit optimized θ_{ref} and fit residuals for χ -transformed catchments (top) and χ_Q -transformed catchments (bottom), for all minimum drainage area thresholds analyzed (see Figure 3 in main text). Color shows basin size: color stretch restricted to emphasize lower drainage areas. Note, each panel is normalized internally such that residuals for each catchment fall between 0 and 1, and residuals scale roughly with catchment size. Thus, relative characteristics between panels are not necessarily comparable and only comparisons within the same panel among catchments of similar sizes are appropriate. Within each panel, we can observe that catchments with anomalous (low) optimized θ_{ref} exhibit similar residuals to catchments with values near 0.5, demonstrating these anomalous values are indeed effective in collapsing profiles and achieving collinearity, and therefore are not the result of relatively inferior fits. Because these catchments also tend to exhibit variable lithology (15, 16) and/or strong disequilibrium, this also demonstrates that adjusting θ_{ref} alone can effectively compensate for and mask meaningful variations in channel steepness.

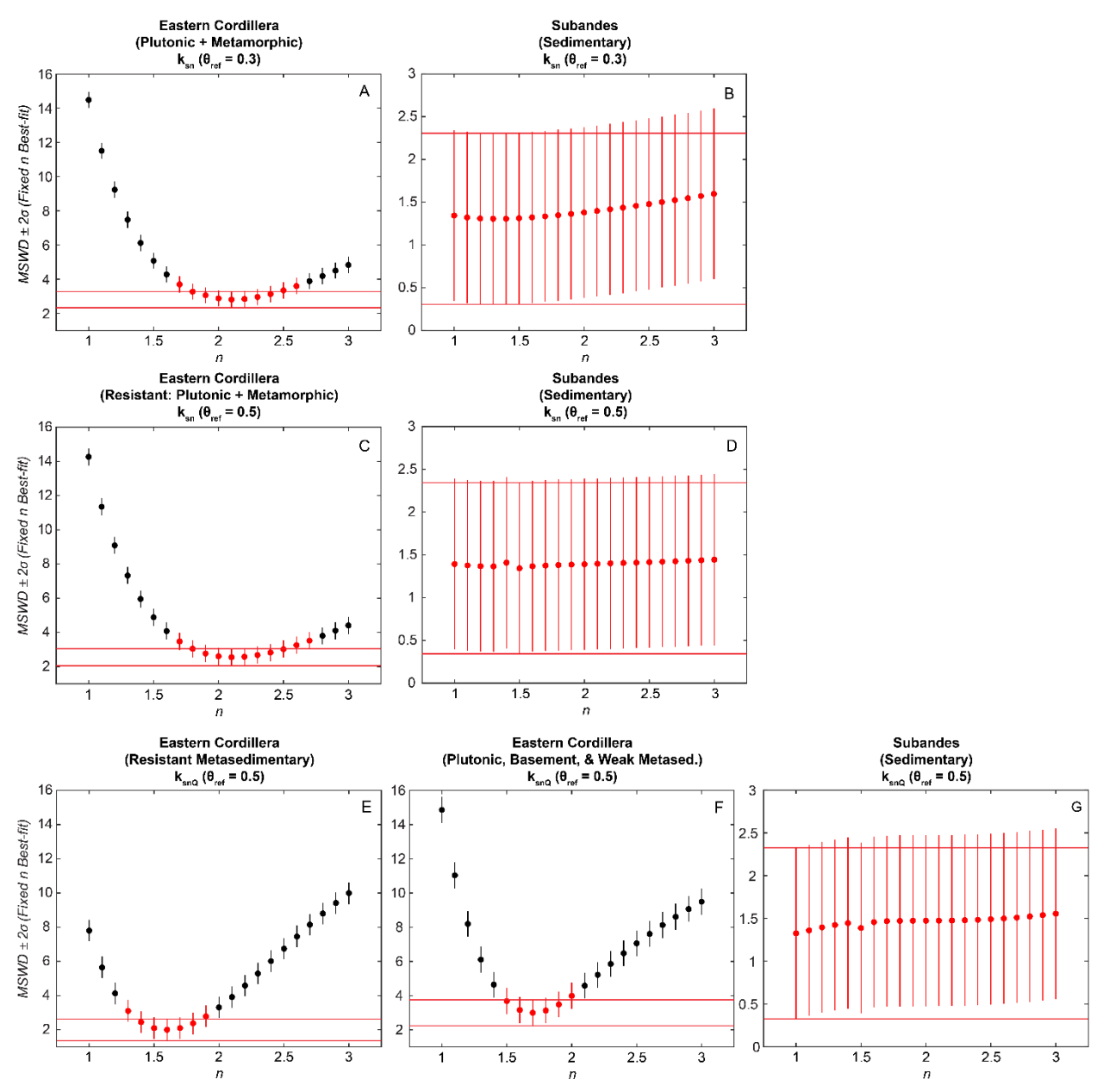


Fig. S2. Constraints on SPM exponent n from regressions for k_{sn} with $\theta_{ref} = 0.3$ (A, B), k_{sn} with $\theta_{ref} = 0.5$ (C, D) and k_{snQ} with $\theta_{ref} = 0.5$ (E-G). Each point records MSWD $\pm 2\sigma$ of best-fit regression (representing a distinct $K(\text{or }K_p)$ -n pair) for given fixed n values, calculated over the range of 1-3 at increments of 0.1 using methods from Adams et al. (1). Red horizontal lines bound MSWD $\pm 2\sigma$ for the n value of the best-fit among all values (MSWD nearest to 1). Regressions for different n values with MSWD range that overlaps with best-fit n value are shown in red and interpreted to yield comparable goodness-of-fit, thus providing constraints on the range of possible n values. Note, n values for Eastern Cordillera (EC) trends evident using k_{sn} (both θ_{ref}) are higher and less well constrained than either of the EC trends that emerge using k_{snQ} . Subandean trends are unconstrained for both k_{sn} and k_{snQ} . However, assuming an n value for Subandean trends equal to those calculated from EC trends, which are compatible with Subandean trends, implies a K or K_p value that can be directly compared.

Data S1. (separate file)

Source data for all plots and analyses presented in the main text, comprising a spreadsheet with three tabs formatted in excel. Tabs are: 1) 'Large Basin Stats' with topographic characterizations of 104 basins depicted in main text Figs. 1 and 3; 2) 'Trunk-Tributary Pairs' with source data and relevant information for all catchments analyzed to create main text Fig. 2; and 3) 'Erosion Rate Catchment Stats' containing all information to reproduce analysis presented in main text Fig. 5.